State of Oregon
Oregon Department of Geology and Mineral Industries
Vicki S. McConnell, State Geologist

USING AIRBORNE THERMAL INFRARED AND LIDAR IMAGERY TO SEARCH FOR GEOTHERMAL ANOMALIES IN OREGON

BY IAN P. MADIN[1], JOHN T. ENGLISH[2], PAUL A. FERRO[3], CLARK A. NIEWENDORP[1]

2013

Oregon Department of Geology and Mineral Industries; 2, City of Hillsboro, Oregon; 3, Port of Portland, Oregon

OREGON DEPARTMENT OF GEOLOGY AND MINERAL INDUSTRIES, 800 NE OREGON STREET, #28, SUITE 965, PORTLAND, OR 97232

DISCLAIMER

This report was prepared as an account of work sponsored by an agency of the United States Government. Neither the United States Government nor any agency thereof, nor any of their employees, makes any warranty, express or implied, or assumes any legal liability or responsibility for the accuracy, completeness, or usefulness of any information, apparatus, product, or process disclosed, or represents that its use would not infringe privately owned rights. Reference herein to any specific commercial product, process, or service by trade name, trademark, manufacturer, or otherwise does not necessarily constitute or imply its endorsement, recommendation, or favoring by the United States Government or any agency thereof. The views and opinions of authors expressed herein do not necessarily state or reflect those of the United States Government or any agency thereof.

This report does not constitute a standard, specification, or regulation.

This product is for informational purposes and may not have been prepared for or be suitable for legal, engineering, or surveying purposes. Users of this information should review or consult the primary data and information sources to ascertain the usability of the information. This publication cannot substitute for site-specific investigations by qualified practitioners. Site-specific data may give results that differ from the results shown in the publication.

For additional information:
Administrative Offices
800 NE Oregon Street #28, Suite 965
Portland, OR 97232
Telephone (971) 673-1555
Fax (971) 673-1562
http://www.oregongeology.org
http://egov.oregon.gov/DOGAMI/

USING AIRBORNE THERMAL INFRARED AND LIDAR IMAGERY TO SEARCH FOR GEOTHERMAL ANOMALIES IN OREGON

TABLE OF CONTENTS

LIST OF TABLES

LIST OF FIGURES

1.0 INTRODUCTION

The Oregon Department of Geology and Mineral Industries (DOGAMI), together with the states of Idaho, Utah, and Nevada formed the Great Basin Consortium, and as participants in the National Geothermal Data System (NGDS) project, this consortium received supplemental federal assistance funds from the US Energy Department's (USDoE) Geothermal Technologies Program through the Arizona Geological Survey for new geothermal data collection (expanding Task 2.4 of the project objectives). DOGAMI's portion of the federal assistance funds supported the following work:

- Pilot study – airborne thermal infrared (TIR) imagery with co-acquired lidar topographic imagery.
- The drilling of three thermal gradient wells (Niewendorp, 2013).

This report, *Using Airborne Thermal Infrared and lidar imagery to search for geothermal anomalies in Oregon*, was prepared by Oregon Department of Geology and Mineral Industries (DOGAMI) to partially satisfy Task 2 of the TIR pilot study's Scope of Work, and to provide preliminary analysis of the data TIR and lidar.

As described in Niewendorp and others (2013), the TIR pilot study advanced through five (5) phases that included selection of the TIR/lidar flight areas, development of the initial proposal, State and federal permitting, bidding, and the collection of the TIR/lidar data and processing. That process resulted in the collection of the entire proposed data set, covering five target areas shown in Figure 1.1. The initial goal was to acquire the TIR and lidar early enough to be able to use the results to site the thermal gradient holes, that proved impractical given the time constraints of permitting and bidding both contracts. In the end, all three holes fall within the footprint of the imagery acquisitions at sites dictated largely by permitting expedience. The imagery collected is a rich, voluminous and complex data set, and we realized that it is not simply a matter of looking at a visualization and picking the hot spots. It required substantial reprocessing of data, integration of other data sets and experimentation to develop useful results. Accordingly our limited budget for analysis only covered the Summer Lake pilot study area (Figure 1.1). Summer Lake was chosen because it contained one of our drill sites and because it contained known warm springs that would provide a test of the method. Future work should include both the analysis of the four remaining data sets, and field work to ground check the various possible thermal anomalies that were identified.

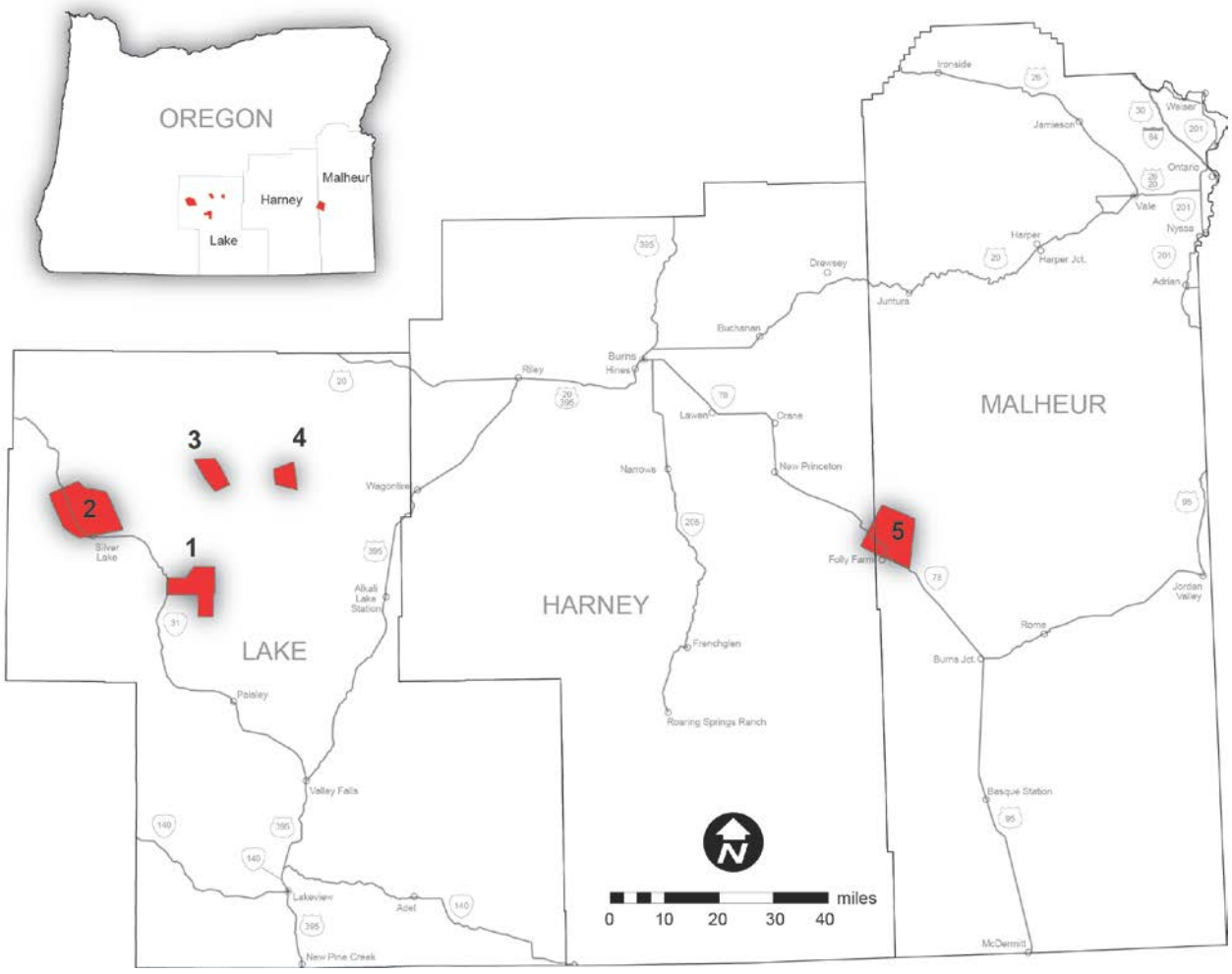

Figure 1.1: Location of TIR/Lidar project areas in parts of Lake, Harney, and Malheur counties. Numbers are keyed to flight areas as follows; 1) North Summer Lake and area of interest for this study, 2) Paulina Marsh, 3) Christmas Valley, 4) Oregon Military Department (Sector 6), and 5) Baker Pass. Combined the five flight areas represented 257 square miles

1.1 PURPOSE OF THE PROJECT

Remotely sensed thermal infrared (TIR) imagery has been used in geothermal exploration for decades. Studies have used both airborne (Seielstad and Queen, 2009; Lee, 1978; Hodder, 1970; Mongillo, 1994; Haselswimmer and others, 2011) and satellite based imagery (Coolbaugh and others, 2007; Eneva and others, 2006) to look for warm ground and thermal features. Many others have used TIR imagery to map alteration and precipitation mineralogy associated with thermal water (Kratt and others, 2006; Hellman and Ramsey, 2004; Vaughn and others, 2005). Although many of the studies that use airborne data to look for thermal features have been quite successful, they have typically been looking for relatively high temperature anomalies (Seielstad and others, 2009; Haselwimmer and others, 2011). Our goal with this project was to test whether TIR data with very high spatial resolution and accuracy could be used to identify warm springs or ground that was only slightly warmer than background levels. The other unique aspect of this study was the combination of high resolution lidar topographic

imagery with the TIR imagery. The lidar provided a basemap to orthorectify the TIR to provide a high degree of spatial accuracy for the TIR, and the lidar provided a wealth of information about factors like vegetation, water, and geomorphology that influence the TIR values. Although studies have coupled lidar and TIR imagery for analysis of water temperature in streams or have overlaid independently-collected lidar with TIR imagery (Jaworowski and others, 2009) we believe that this is one of the first attempts to co-acquire TIR and lidar imagery in order to be able to merge them into a high resolution-high accuracy project.

2.0 DATA CHARACTERISTICS

2.1 CHARACTERISTICS OF TIR DATA

Digital TIR imagery and high resolution lidar imagery were collected for the Summer Lake pilot area shown in Figure 2.1. The TIR and lidar imagery were co-acquired (both instruments operating simultaneously in the aircraft) on a calm, clear night (March 4, 2012) during the winter in order to minimize solar heating effects that might swamp low thermal amplitude geothermal signals. Ambient temperatures at the time of acquisition ranged from -5 to -8 C. The technical characteristics of the TIR and lidar data are summarized in Table 2.1.

Table 2.1: Technical Specification of TIR and Lidar data

Data Specifications						
	Thermal accuracy, Tk/Tr, n=6	Consistency (image to image or swath to swath)	Native Resolution	Vertical Accuracy	Horizontal Accuracy	Delivered Grid Resolution
TIR	2.4 C RMSE	.5 C	.5 M		.5m RMSE	.5 m
Lidar		1 cm	5.4 pulse/m^2	2.3 cm RMSE		1 m

The raw thermal radiance images were trimmed, orthorectified using the lidar data and mosaiced to produce a seamless, spatially accurate radiance image of the study area. The radiance values were the converted into temperature values by reference to laboratory instrument calibration and a set of instrumental thermographs collected in the study area during imagery acquisition. The result was a high thermal and spatial resolution, high thermal and spatial accuracy mosaic image of the pilot study area at (Figure 2.1).

Figure 2.1 shows the adjusted radiant temperature, T_r as measured by the instrument system. The system measures the total infrared energy in the 8-9.2 µm wavelength range. This signal consists of energy emitted from the surface, energy reflected by the surface, and energy absorbed and re-emitted by the intervening atmosphere. Flying at night under cold, still conditions minimizes the reflected and re-emitted energy, providing a more accurate map of surface temperature. However, even under the best of circumstances the measured T_r is not a direct measurement of the true surface temperature, or kinetic temperature, T_k. All materials emit infrared radiation with differing emissivity (a measure of efficiency of emission of infrared energy at a particular kinetic temperature relative to a perfect blackbody). So for example, water and pavement that have the same T_k, may have significantly different T_r because they have different emissivity values. Therefore any TIR image is both a map of varying temperature, but also of varying emissivity. The T_r of the image in Figure 2.1 has been adjusted assuming that all parts of the image have the emissivity of water, and is presented with a custom non-linear color ramp provided by the vendor to enhance higher temperature anomalies. The obvious bright features in the image (high relative temperature) are all water bodies, either ponds, marshes,

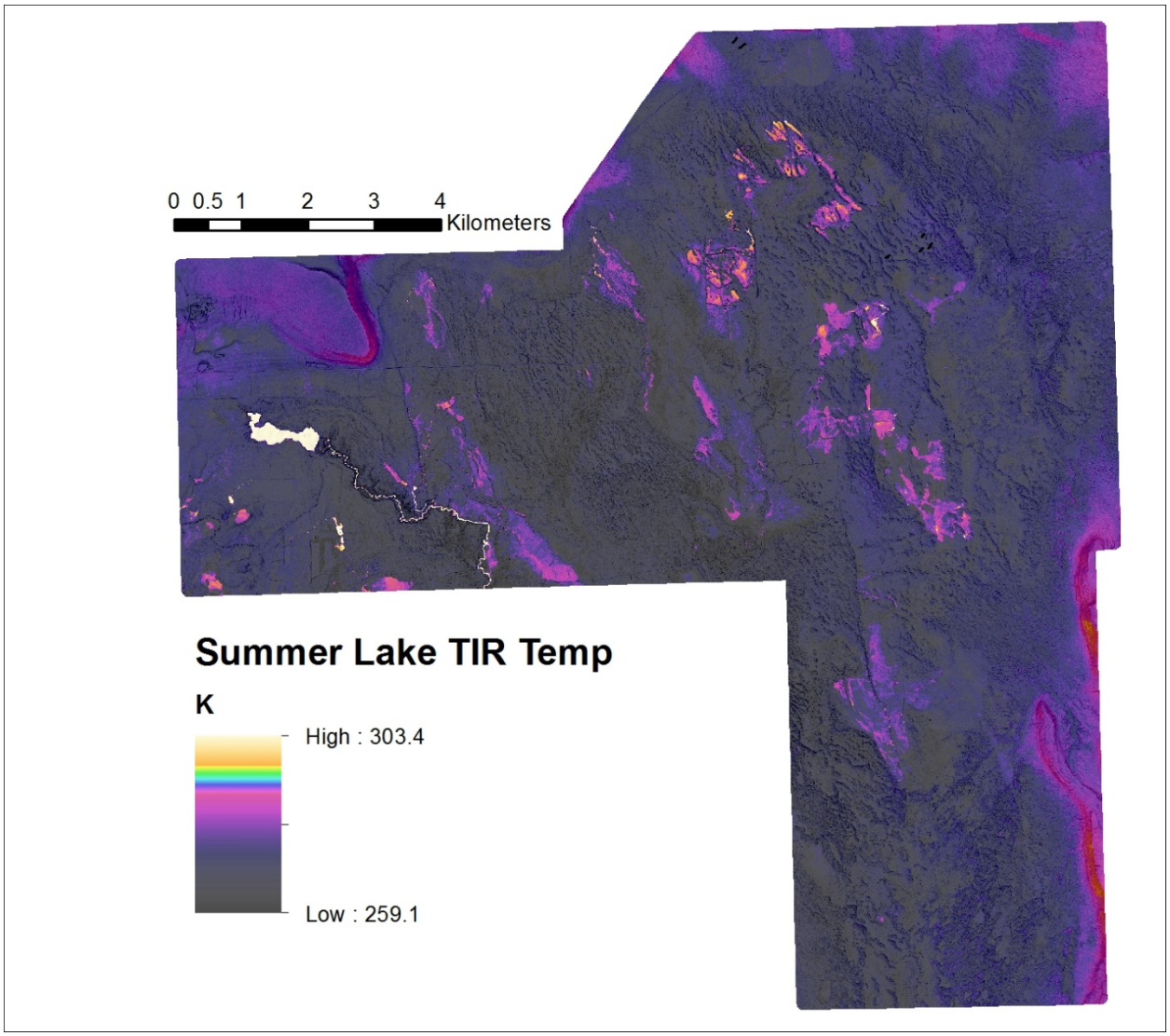

Figure 2.1: Radiant Temperature image of the Summer Lake study area

streams or ditches, or springs. This is because liquid water or even thin ice in contact with liquid water are relatively hot (>= 273 K) against the background land surface temperature (T_r ~265 K, ambient air temperature during the acquisition of Figure 2.1 ranged from 265-268 K). Therefore it is not surprising that Ana Reservoir (average T_r, 285 K), a large spring-fed lake in the NW corner of Figure 2.1, stands out, as do the Ana River downstream of the reservoir and several connected ditches. Figure 2.2 is an enlargement of the area north of Ana Reservoir, in which numerous round patches occur that have a higher T_r relative to the surrounding ground. These features are juniper trees, and their apparent relative warmth (T_r ~ 273 K) may simply be the result of their emissivity relative to the surrounding soil (T_r ~266- 268 K). Although we were unable to locate measured emissivity values for juniper trees, emissivity for pine trees is ~ .982 (http://www.icess.ucsb.edu/modis/EMIS/html/em.htm). Emissivity of soil varies widely, but the emissivity of soils from Death Valley, California, a similar arid playa lake environment, range

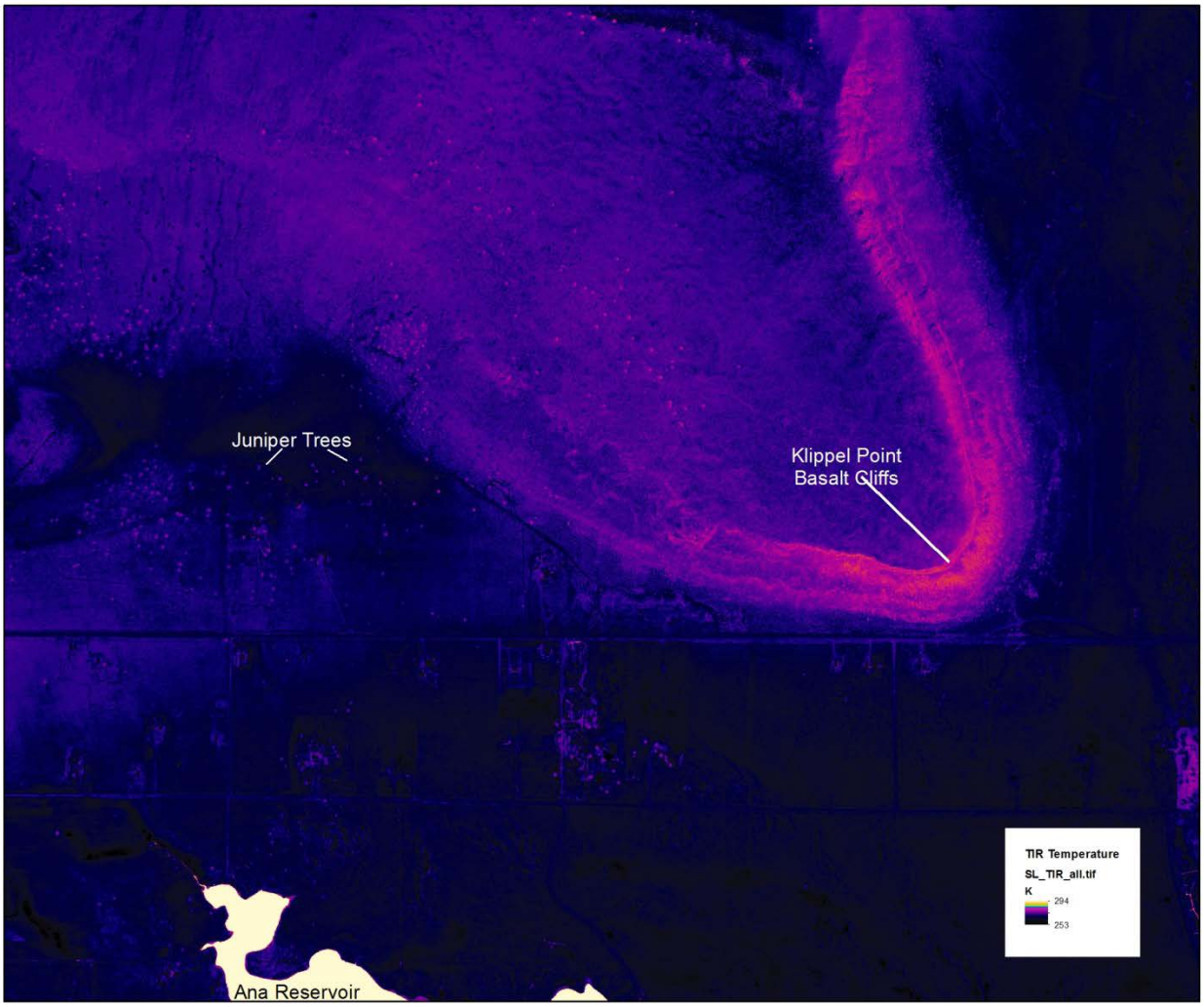

Figure 2.2: Detail of Summer Lake Radiant Temperature image, showing relatively warm values associated with water bodies, juniper trees and basalt cliffs

from ~.85 to .96. Table 2.2 shows the expected radiant temperature for several different materials at the same kinetic temperature.

Table 2.2: Relationship between kinetic and radiant temperature for materials with different emissivity values. Relationship defined by $T_{radiant} = \varepsilon^{1/4} T_{kinetic}$. (Olsen, 2007)

Material	$T_{kinetic}$	ε	$T_{radiant}$
pine	273	0.98	271.6
water	273	0.95	269.5
basalt	273	0.72	251.5
desert soil	273	0.9	265.9

The relationships in Table 2.2 strongly suggest that the apparent high temperature of the juniper trees is a function of their emissivity, not a true temperature difference.

The other striking thermal anomalies in Figures 2.1 and 2.2 besides the relatively warm water features and vegetation are the warm areas associated with bedrock ridges in the SE and NW corner of the figure. Figure 2.2 shows the location of basalt cliffs (Klippel Point) N of Ana Reservoir that have a T_r of ~274 K. This temperature anomaly cannot be explained by a difference in emissivity, as the much lower value for basalt (Table 2.2) should result in significantly lower T_r. One possible explanation for these anomalies is that the generally S and W facing cliffs absorbed more heat from the sun during the day, and are truly much warmer due to that latent heat.

To test this hypothesis, we used the insolation tools in the Spatial Analyst module of ArcMap to calculate total insolation for the day prior to data acquisition. The insolation tool uses information about the sun's position for a particular day and latitude and slope information to calculate the total energy absorbed by each pixel in the image. We resampled the lidar DEM to 5m pixels to speed up the calculation, and then ran the insolation model for the area of Figure 2.3. Figure 2.3 compares the T_r map with the total insolation map, and it is quite clear that there is little correspondence. The NE facing basalt cliffs of Klippel point received dramatically less insolation than the S facing cliffs, but have similar T_r. Several gravel stockpiles in the NW corner of the figure image have stark contrasts in insolation between their north and south sides, but no discernible difference in T_r. Figure 2.4 is a photo of the basalt cliff at Klippel Point, and although the surface is somewhat oxidized, there is no obvious lichen or desert varnish layer that might affect the emissivity. We conclude that the T_r anomalies associated with the basalt cliffs reflects a true T_k anomaly. We speculate that this may be because basalt has a much higher thermal conductivity than the sandy-gravelly colluvium and beach and lake deposits that cover most of the area.

2.2 CHARACTERISTICS OF LIDAR DATA

The lidar imagery was collected in order to help accurately georeference the TIR data and to provide a detailed and accurate paired basemap for analysis of the thermal imagery. The lidar data collected for this project had high accuracy and resolution, corresponding to USGS Quality Level 1 (http://www.dewberry.com/files/pdf/NEEA_Final%20Report_Revised%203.29.12.pdf), although they do not meet the resolution specifications of the vast majority of Oregon lidar collected by the Oregon Lidar Consortium (http://www.oregongeology.org/sub/projects/olc/olc_lidar_spec.pdf). Table 1 summarizes the lidar technical characteristics.

The primary lidar products used for this project were the bare earth and highest hit DEM's illustrated in Figure 2.5. These DEMs have a native resolution of 1 m and were used to orthorectify the TIR data. As a result the correspondence between topographic features in the lidar and their thermal signatures is excellent (Figure 2.6). For analytical purposes, we created new DEMs from the lidar point data with a resolution of .5 m. These grids are detailed enough to resolve fine features of vegetation such as grasses and sagebrush.

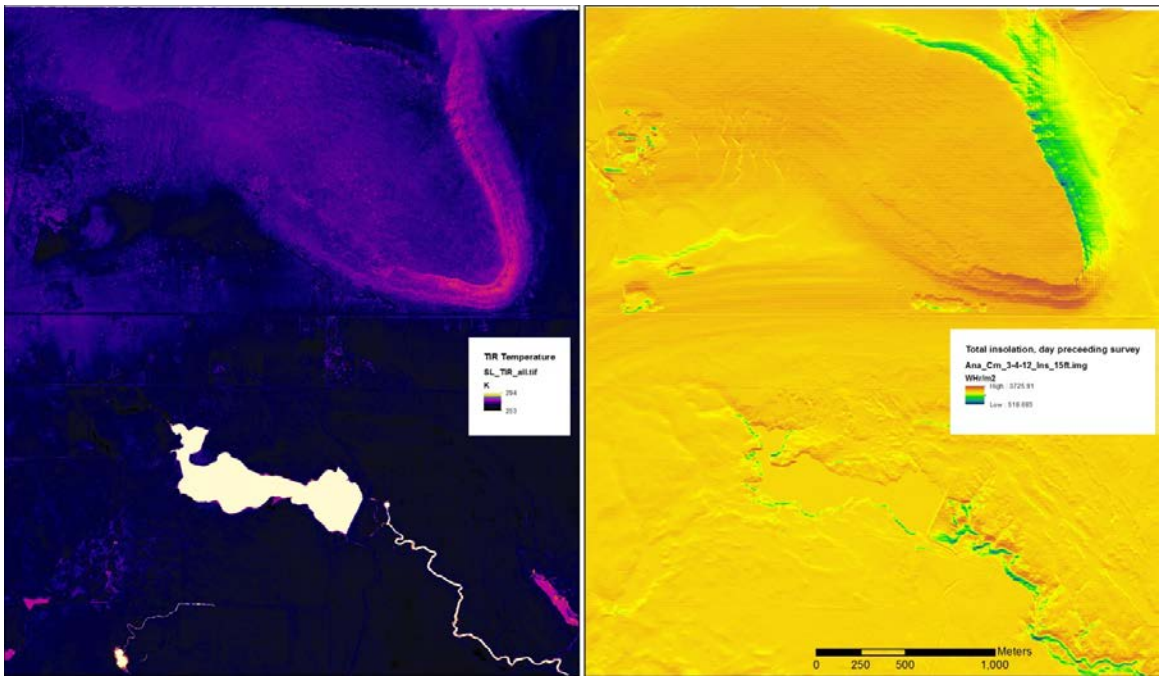

Figure 2.3: Test of the influence of insolation on radiant temperature. Left image shows radiant temperature, right image shows total insolation for the day preceding acquisition

Figure 2.4: photograph of basalt cliff at Klippel point

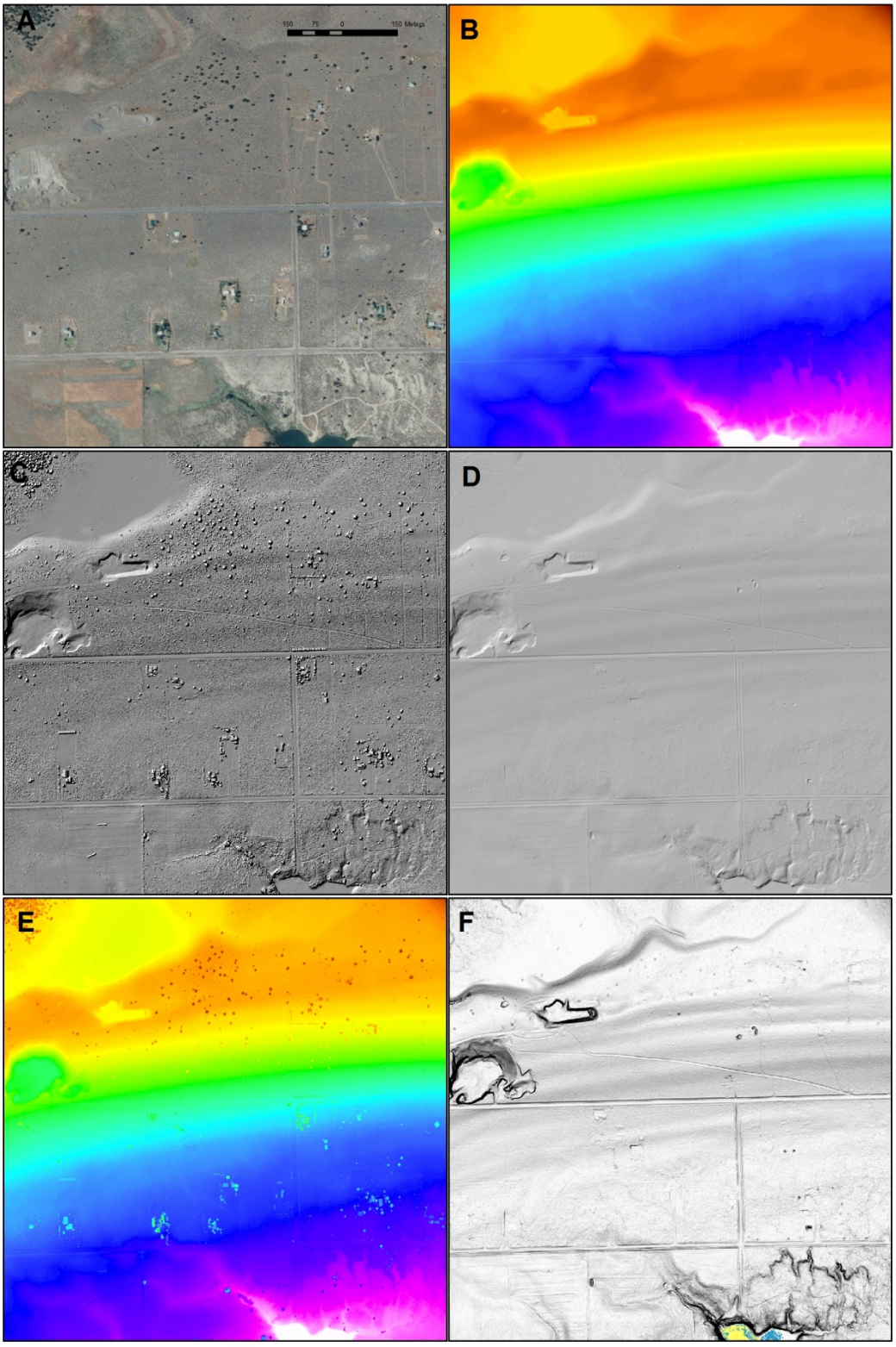

Figure 2.5: Example of lidar imagery. A) Orthophoto; B) Lidar base earth elevation; C) Lidar highest hit hillshade; D) Lidar bare earth hillshade; E) Lidar highest hit elevation; and F) Lidar bare earth slopeshade

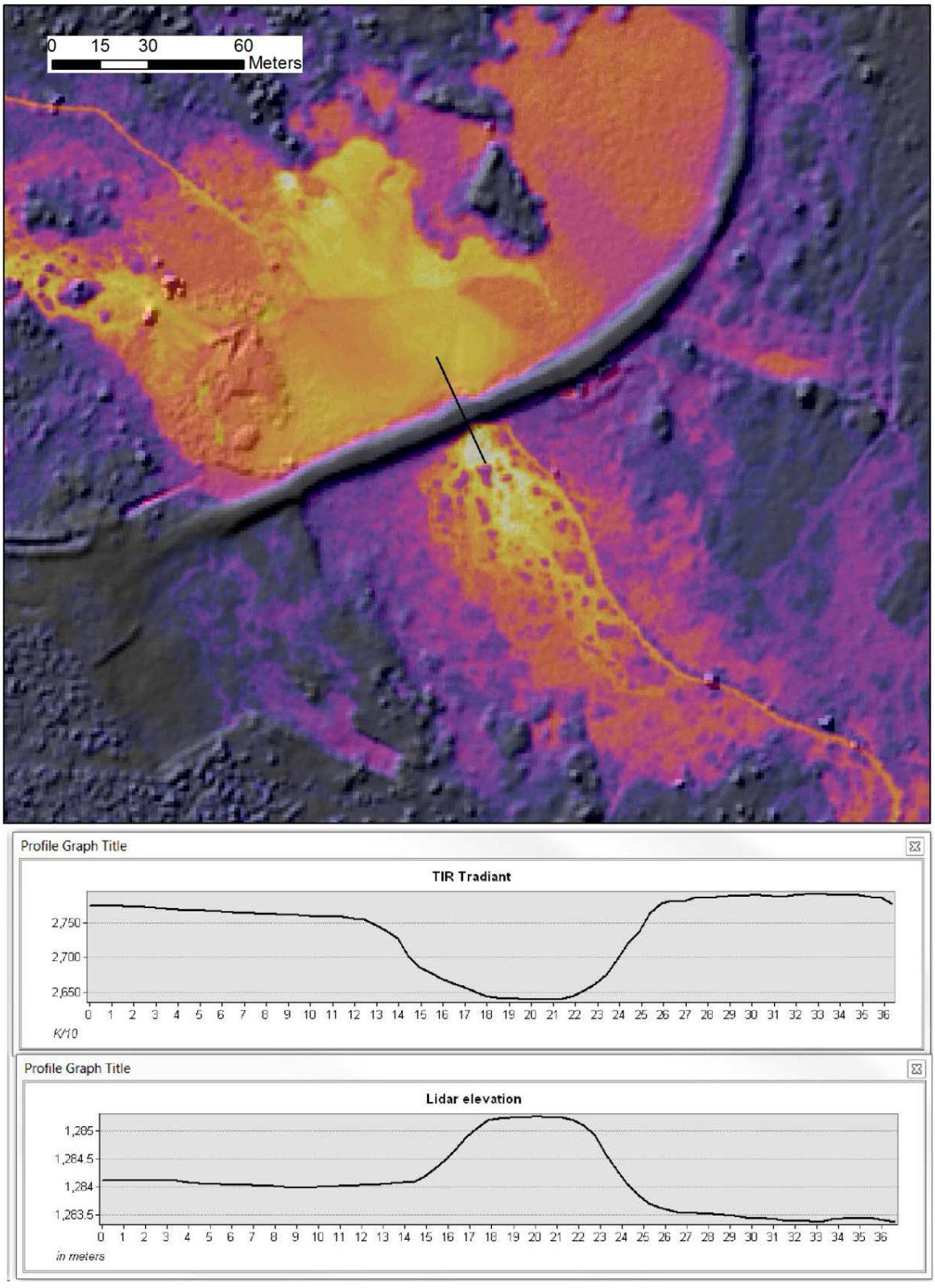

Figure 2.6: Illustration of the spatial registration of TIR and lidar imagery. Top image shows TIR image draped on lidar slopeshade, black line is location of profile crossing dike separating two relatively warm water bodies. Profiles across dike show close registration of image sets.

3.0 ANALYSIS

3.1 IDENTIFICATION OF WARM SPRINGS FROM TIR DATA

In order to find all possible thermal springs in the image, we extracted all cells with values greater than 285 K (12 C, the typical temperature of groundwater in the region, and also of the Ana Reservoir during the flight) from the raster mosaic for the entire study area (area of Figure 2.1), then converted those raster cells into points, which makes it possible to locate individual cells with high temperature that may be visually lost in the larger image. This made it possible to identify numerous warm springs (defined here as above 286 K or 13 C) by analyzing the distribution of temperature values from the TIR image and the underlying topography as defined by the lidar data. We also selected all values between 276 K and 285 K and converted those cells to points, and searched that data for cold springs.

Figure 3.1 shows how the combined data sets define warm and cold springs. We found 37 warm springs with temperatures ranging up to 21.4 C, and 81 cold springs, as shown in Figure 3.2. In addition to terrestrial springs, the imagery identified plumes of warm surface water in Ana Reservoir, probably due to submerged warm springs (Figure 3.3). Limited field time and lack of access to private property made it difficult to field check any of the located springs. Temperatures were collected in May of 2013 at three cold spring sites and all measured temperatures were within a degree of the TIR radiant temperature. Existing warm springs databases (GTILO 2; Niewendorp and others, 2012) showed two sets of warm springs in the study area. The database showed four sites in the "Buckhorn Springs" group near Ana Reservoir, only one of which had a recorded temperature (20 C).

The TIR image identified three springs within a few hundred meters of the GTILO sites, but clearly showed that none of the GTILO locations was accurate. The TIR springs had temperatures of 14, 15 and 17 C. In the SE corner of the study area, the GTILO database identified two "Lost Cabin" cabin springs, one with a recorded temperature of 20 C the other with no temperature record. The TIR data identified two cool springs within 100 M of the GTILO springs, but no warm springs within almost 2 km. This suggests that the GTILO records are incorrect, that the springs have cooled over time, or that the springs are warm but have such low flow rates that they do not appear warm in sub-zero weather.

3.2 IDENTIFICATION OF QUATERNARY FAULTS FROM LIDAR DATA

Active geothermal systems are commonly associated with faults in the Basin and Range region, and those faults are often ones that have been active in geologically recent time. Repeated movement on faults during periodic late Pleistocene and Holocene earthquakes may serve to refresh geothermal circulation that has been reduced by the precipitation of minerals from geothermal fluids. Lidar topographic data are particularly well-suited for finding Quaternary or Holocene fault scarps. We visually analyzed the lidar data using a slopeshade visualization at

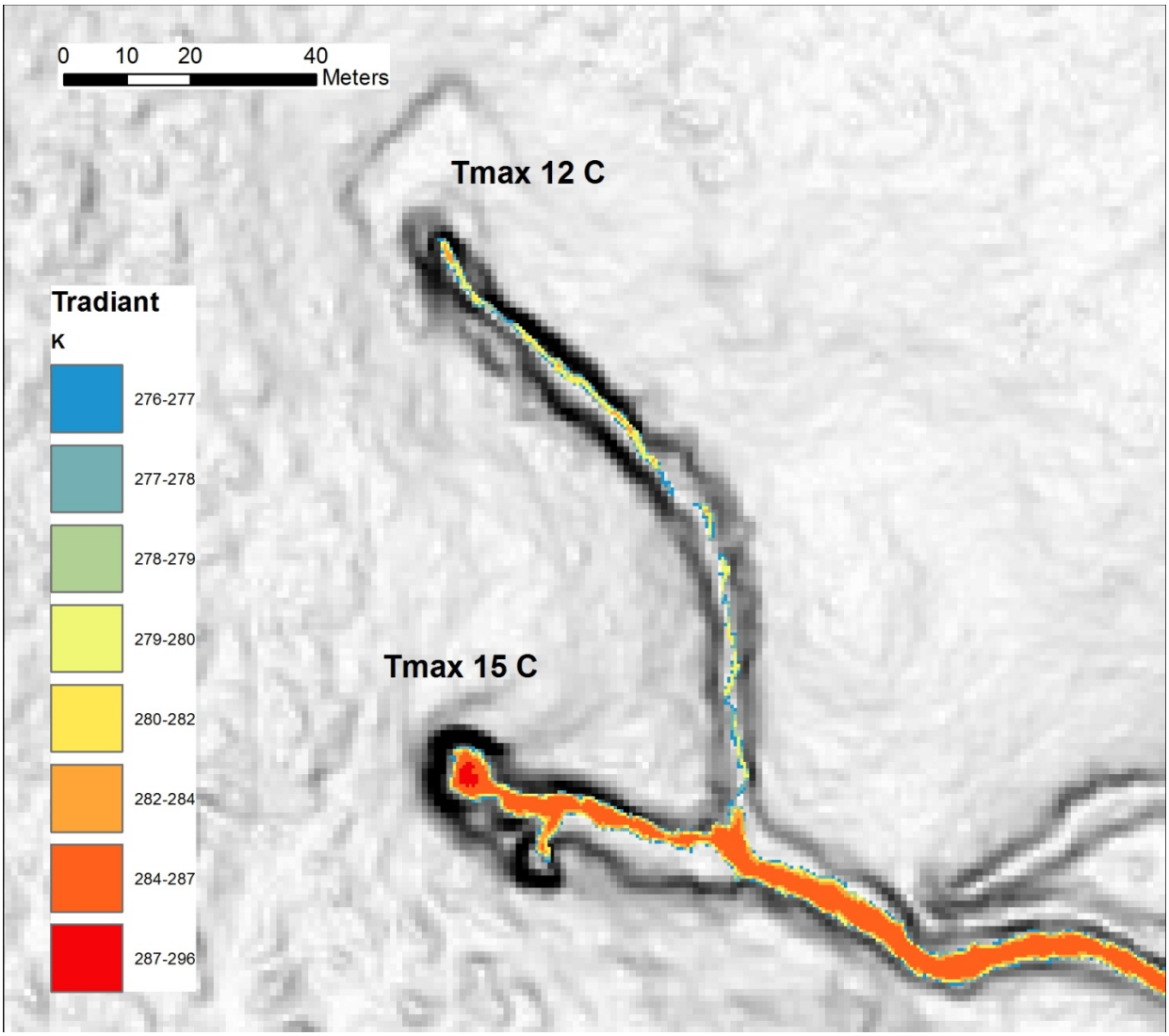

Figure 3.1: TIR pixels with values > 276 K draped on lidar slopeshade image. Combination of temperature patterns and topography defines cool and warm springs

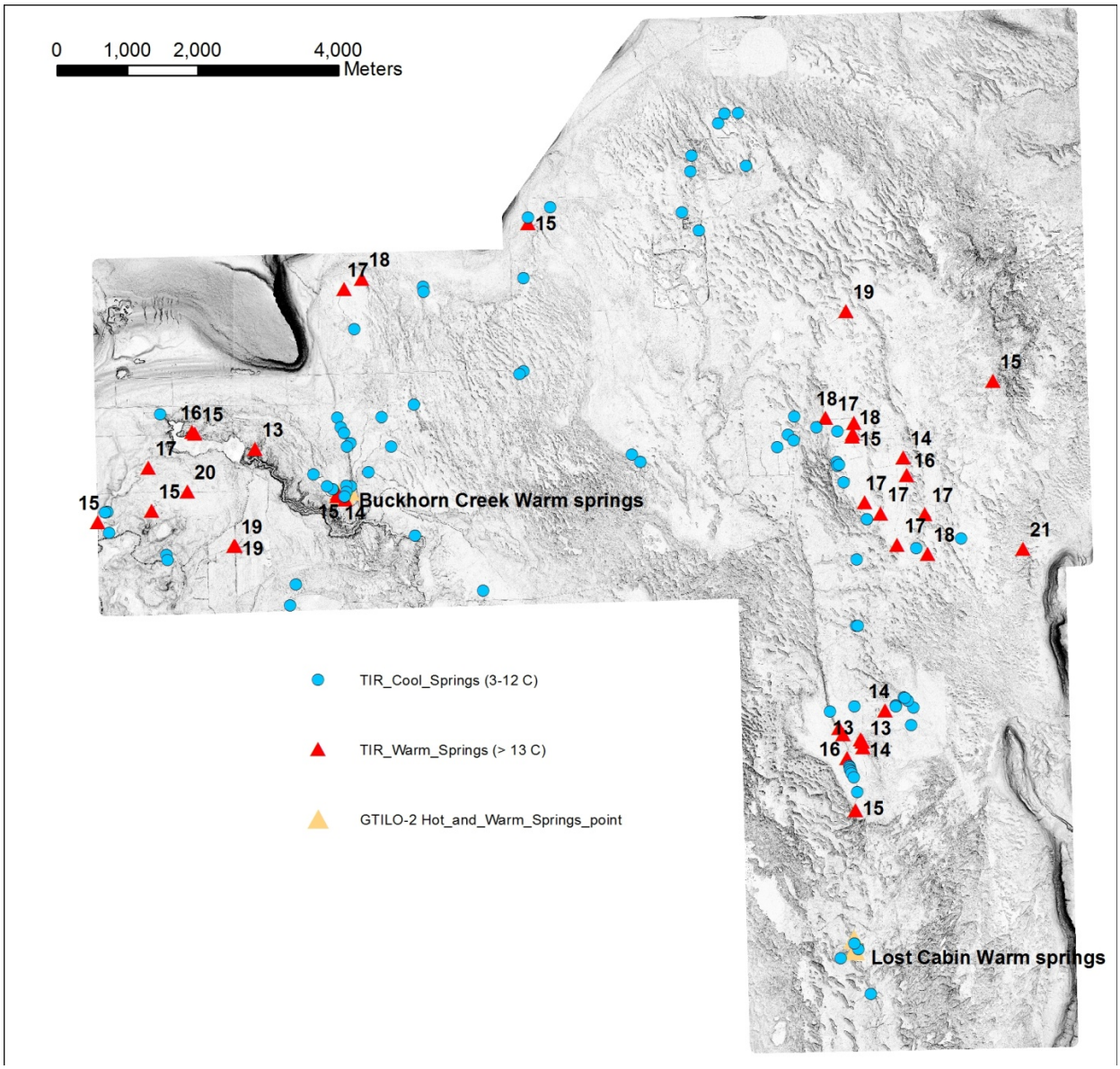

Figure 3.2: Location of cold and warm springs located by TIR data, and previously known warm springs. TIR warm springs labeled with temperature in C

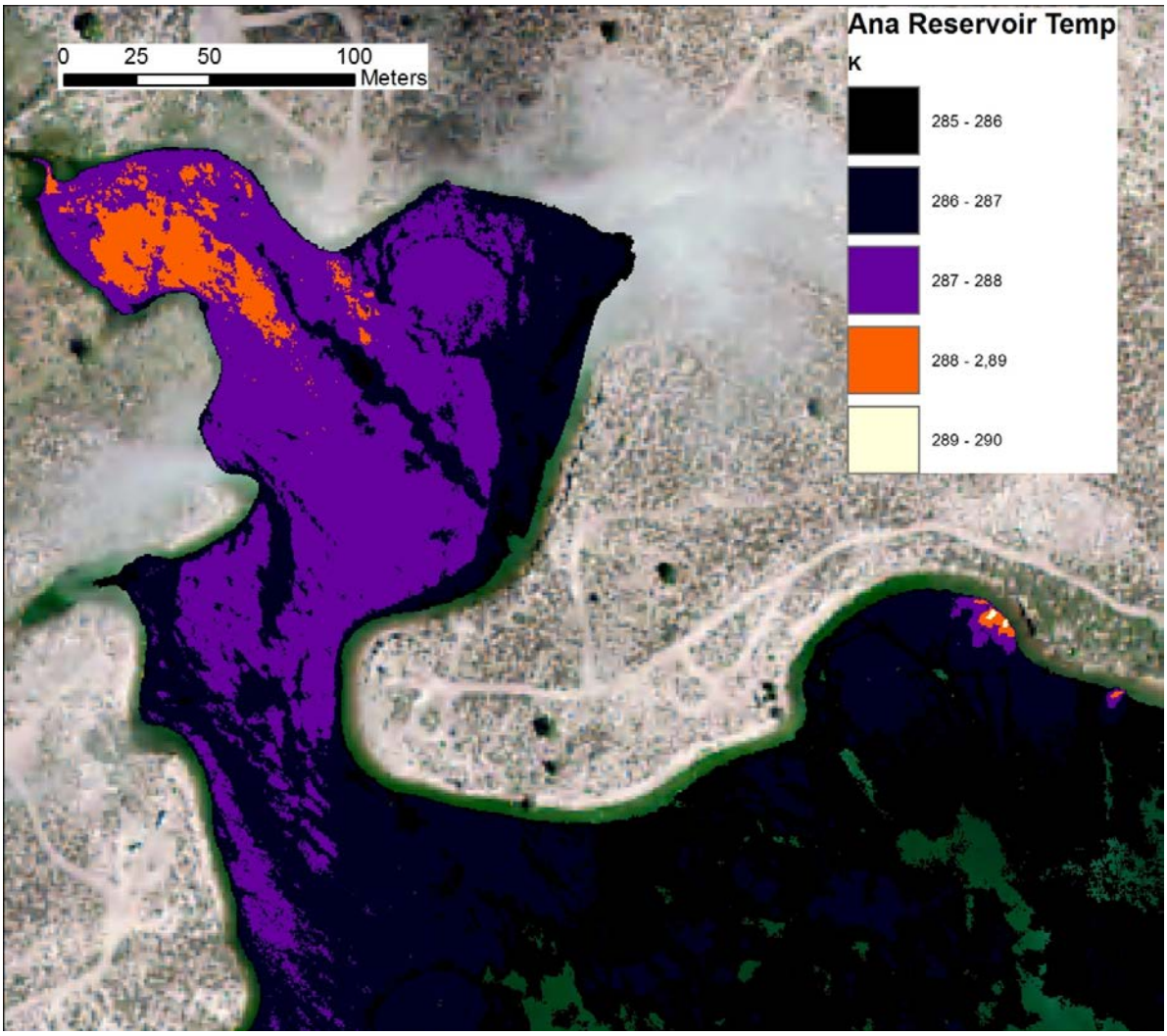

Figure 3.3: TIR image of surface of Ana Reservoir showing warm plumes associated with submerged warm springs of cold and warm springs

scales of 1:8000-1:4,000. A slopeshade visualization (Figure 2.5, 3.4) applies a grayscale color value to each pixel depending on slope, with flat areas white and vertical areas black. In contrast to the commonly-used hillshade visualization of topographic DEMs, the slopeshade does not depend on an illumination azimuth, and is very sensitive to changes in slope, such as a Quaternary fault scarp. Figure 3.4 shows the lidar imagery for the study area, along with the fault scarps identified and a generalized contour at 1307 m. Licciardi (2001) reports an age of ~ 12 ka for the pluvial Lake Chewaucan shoreline developed at this altitude, so

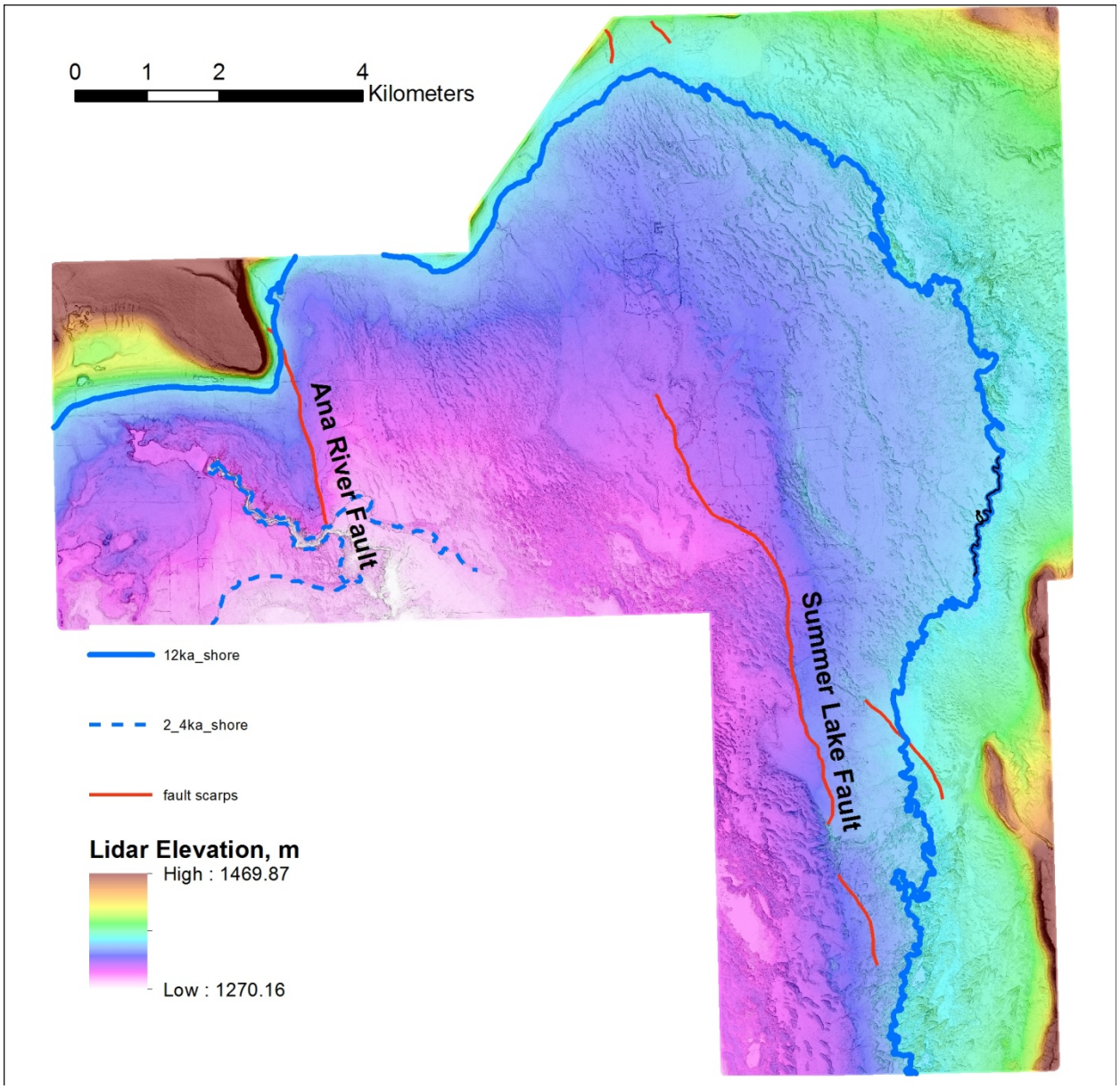

Figure 3.4: TIR Lidar image of study area (color elevation gradient over slopeshade) showing late Quaternary-Holocene fault scarps and select paleo shorelines

the contour provides a time marker for the fault scarps. The Ana river fault in the NW corner of the image is an east-dipping normal fault that is well known, and Langridge and others (2001) trenched the fault and recognized 6 events in the past 100,000 years, including two that post date the most recent maximum lake stand. Langridge and others (2001) also report that the Ana River Fault scarp is truncated by a neo pluvial shoreline between 2000 and 4000 years of age. They calculated slip rates as high as .29 mm/yr.

The Summer Lake Fault is a west-dipping normal fault located in the eastern half of the study area, and trends NNW across floor of the Summer Lake playa for at least 8.5 km. Although the topography along the fault is chaotic in many areas due to sand dunes, the fault locally has a clear, sharp scarp and is associated with a long-wavelength topographic step (Figure 3.5). Bennet and Madin (2012) report scarp heights of up to 6-8m. The orientation of the scarp raises the possibility that it is instead a lake shoreline, but Figure 3.4 shows that the fault clearly crosses the 12 ka shoreline defined by the 1307 m contour. This means that the scarp is not a shoreline, and that the earthquake or earthquakes the created the scarp postdate 12 ka. The range of slip rates for the fault is 0.5 to 0.75 mm/yr. Additional short scarp segments were identified (Figure 3.4), one to the SE of the Summer Lake fault is a west-dipping normal fault that extends for ~1.75 km with a maximum scarp height of ~ 1m. This fault cuts the 12 ka shoreline suggesting at least one event since that date.

At the northern edge of the study area, two parallel scarps define a small graben that extends about a half a kilometer but is lost off the edge of the imagery. Both faults trend NNW, and the easternmost fault is a west-dipping normal fault while the western fault dips east.. The height of both scarps is ~ 0.5 m, and both are entirely above the 12 ka shoreline so their age is poorly constrained.

3.3 IDENTIFICATION OF GEOLOGIC THERMAL ANOMALIES

We analyzed the data to see if we could identify areas where the ground surface was actually warmer than surrounding areas as a result of geothermal activity. We expect any such anomalies to have relatively low thermal amplitude and long spatial wavelengths (100's of m). Therefore, the first step in our analysis was to try to remove the high-thermal amplitude, short spatial wavelength anomalies associated with vegetation, water bodies, roads and structures. To do this we used the lidar data and existing orthophotos to create a series of masks, as shown in Figure 3.6.

3.3.1 Vegetation mask

Masks were created in order to remove TIR values associated with vegetation that would otherwise obstruct visualization of potential geothermal hotspots. Three vegetation masks were created to remove values from the data. The first mask focused on removal of vegetation based on canopy height above the bare earth surface, the second mask's focused on removing vegetation based on surface roughness in the lidar highest hit data, and the third mask aimed to remove low vegetation associated with wetlands and short grasses using color values in orthophotos.

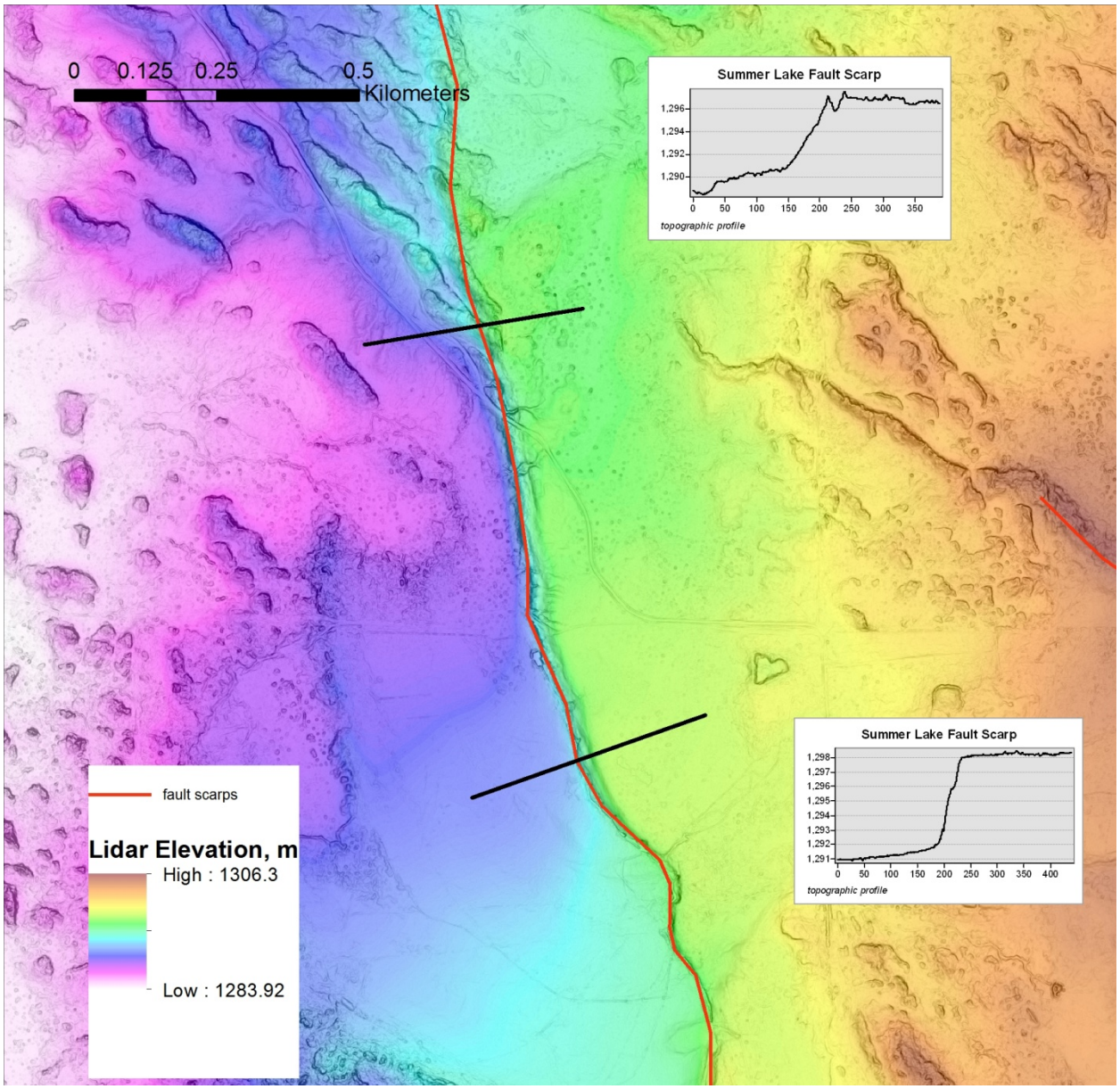

Figure 3.5: Detail of Summer Lake Fault scarp. Lidar elevation gradient over slopeshade. Dark lines mark locations of topographic profiles across scarp

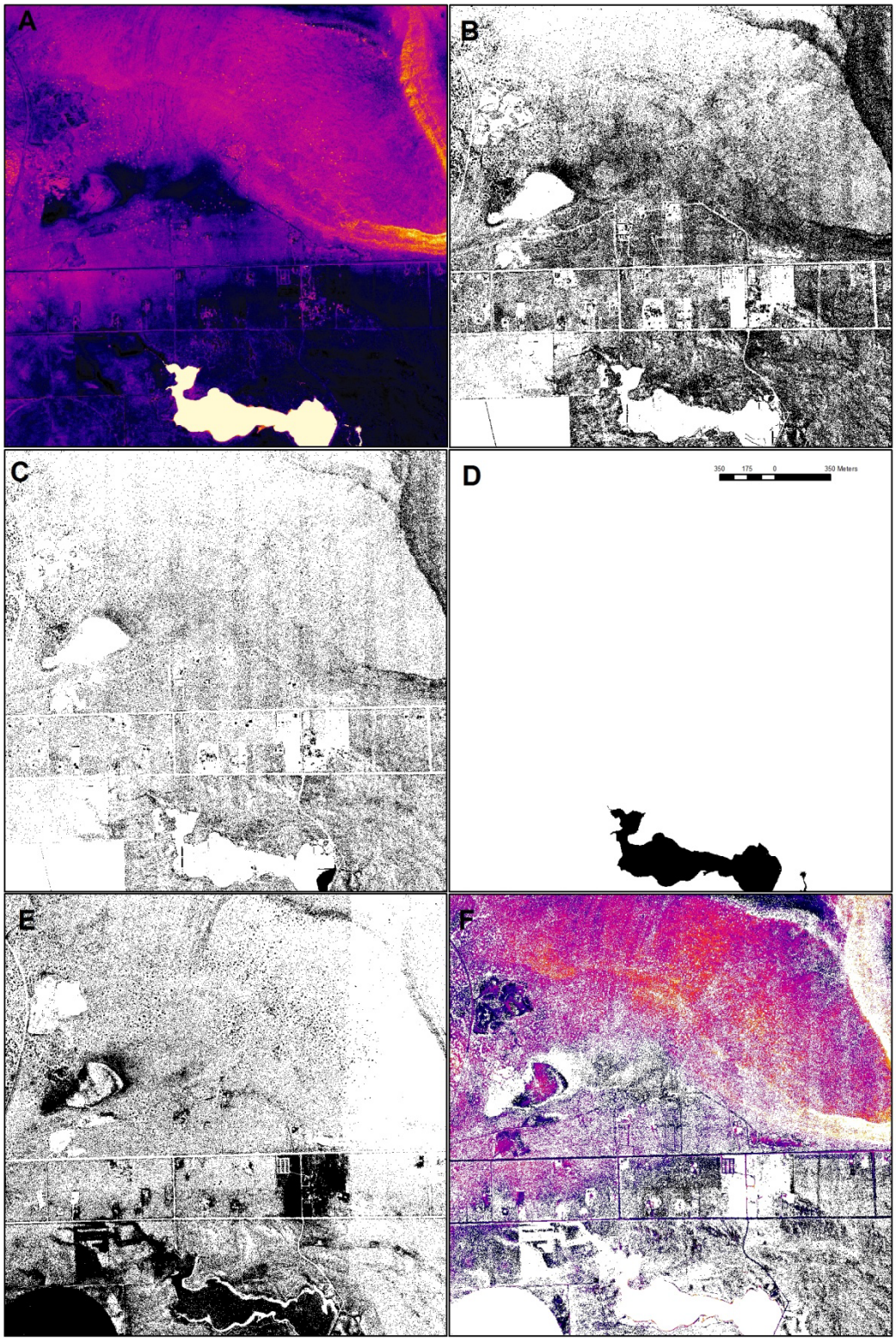

Figure 3.6: TIR masking. A, full TIR image; ZB, canopy vegetation mask; C, roughness vegetation mask; D, water mask; E, NDVI vegetation mask; F, final masked TIR

The canopy height vegetation mask was constructed by first regridding the lidar first–return and ground points to a 0.5 m resolution DEM, then subtracting the resulting bare earth DEM from the highest hit DEM to create a vegetation height model (canopy model). Cell values of the vegetation model greater than 0.2 meters were extracted as a binary integer raster with values of 1 indicating vegetation and values of 0 as not vegetation. Canopy model values less than 0.2 meters were not used as these lower values picked up internal sensor noise and the resulting mask was unreliable.

The second vegetation mask was created using a roughness analysis of the 0.5 m resolution highest hit DEM. Roughness analysis is performed by using the standard deviation of slope derived from a DEM. Roughness values greater than 4.5 were extracted to a binary raster (1=vegetation, 0=not vegetation).

The third vegetation mask was created though a Normalized Difference Vegetation Index (NDVI) analysis of 2009 4-band (RGB-IR) NAIP imagery. NDVI analysis was performed using the NDVI tool found in the ArcGIS Image Analysis Window. NDVI values greater than 100 were used to identify vegetation and extracted as a binary raster (1=vegetation, 0=no vegetation).

The three vegetation masks were used to set intersecting TIR pixel values to null using the "Set Null" tool in ArcGIS spatial Analyst. The resulting raster displayed TIR values only for unvegetated ground.

3.3.2 **Water body mask**

We created a water body mask by starting with available digital stream, ditch and lake data from the NHD, and hand-editing it by reference to 2009 and 2011 one meter resolution orthophotos and the 0.5 m lidar DEMs. The resultant mask is shown in Figure 3.6.

3.3.3 **Masked T_r image**

Figure 3.7 shows the raw masked radiant temperature mask for the pilot area. Masking removed 43% of the pixels, and should result in an image that shows radiant temperature values for rock and soil. Because so much data was removed, and because we were searching for targets with long spatial wavelengths, we use a square moving-window mean filter 100 m long on a side to smooth the data and fill in masked areas. The resulting filtered image is shown in Figure 3.8. This image provides a much simpler picture of temperature anomalies that are likely to be related either to variations in soil or rock emissivity values, or temperature variations related to soil or rock type of localized geothermal heat. We have identified 6 different types of apparent thermal anomalies on Figure 3.8. The anomalies labeled A occur in every location where basalt bedrock is at or near the surface. As discussed earlier, this does not seem likely to be the result of emissivity or insolation contrasts, and may be related to the lack of insulating soil or sediment cover. These anomalies are very large, typically 6-10 K above the background T_r (265 K).

The anomalies labeled B are all associated with areas with abundant surface water and are typically about 8 degrees C (273 K) above the background.. Ground in these areas may actually be warmer due to the presence of relatively warm (285 K) ground water near the surface, but it is

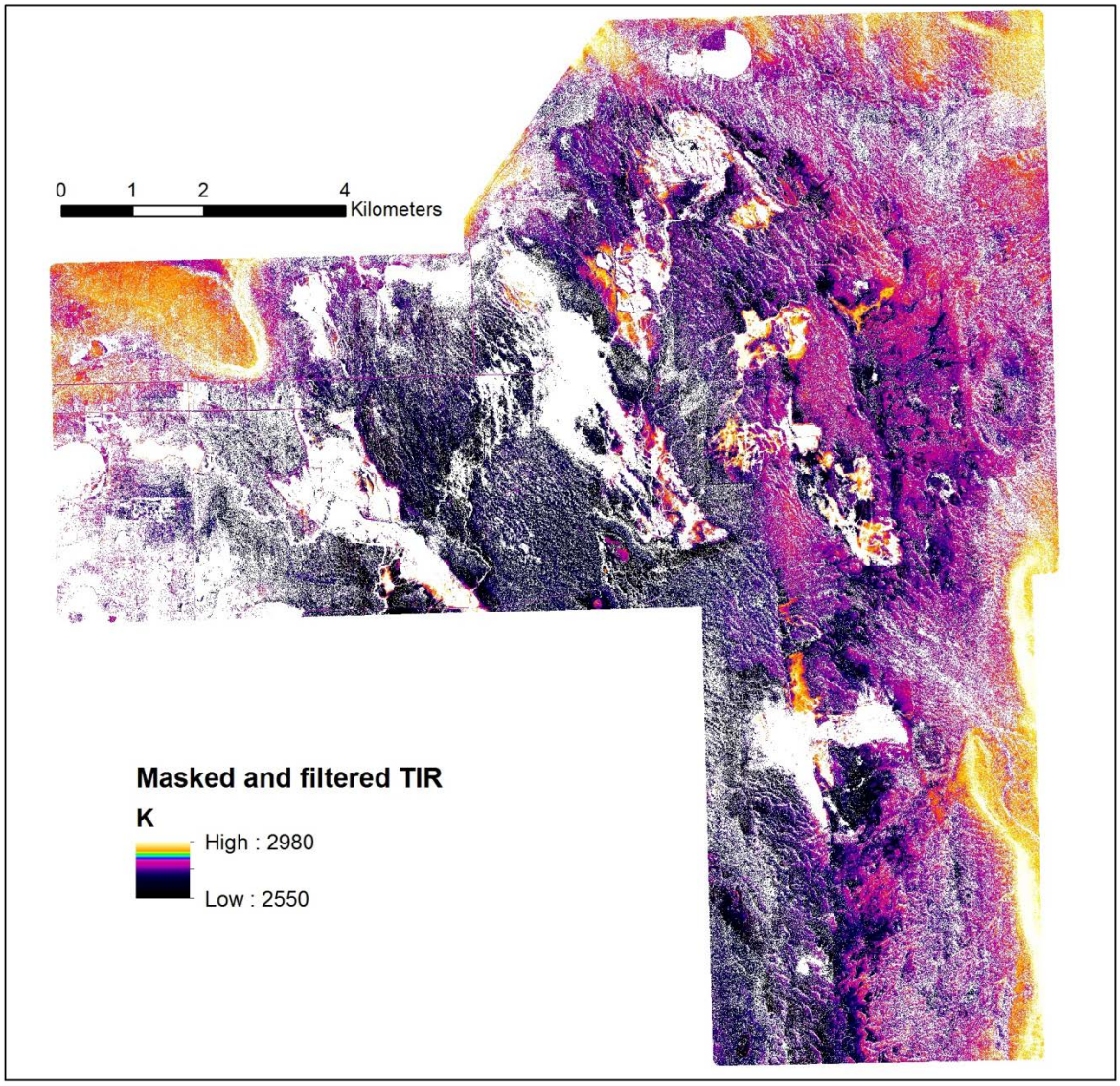

Figure 3.7: Masked TIR image of study area

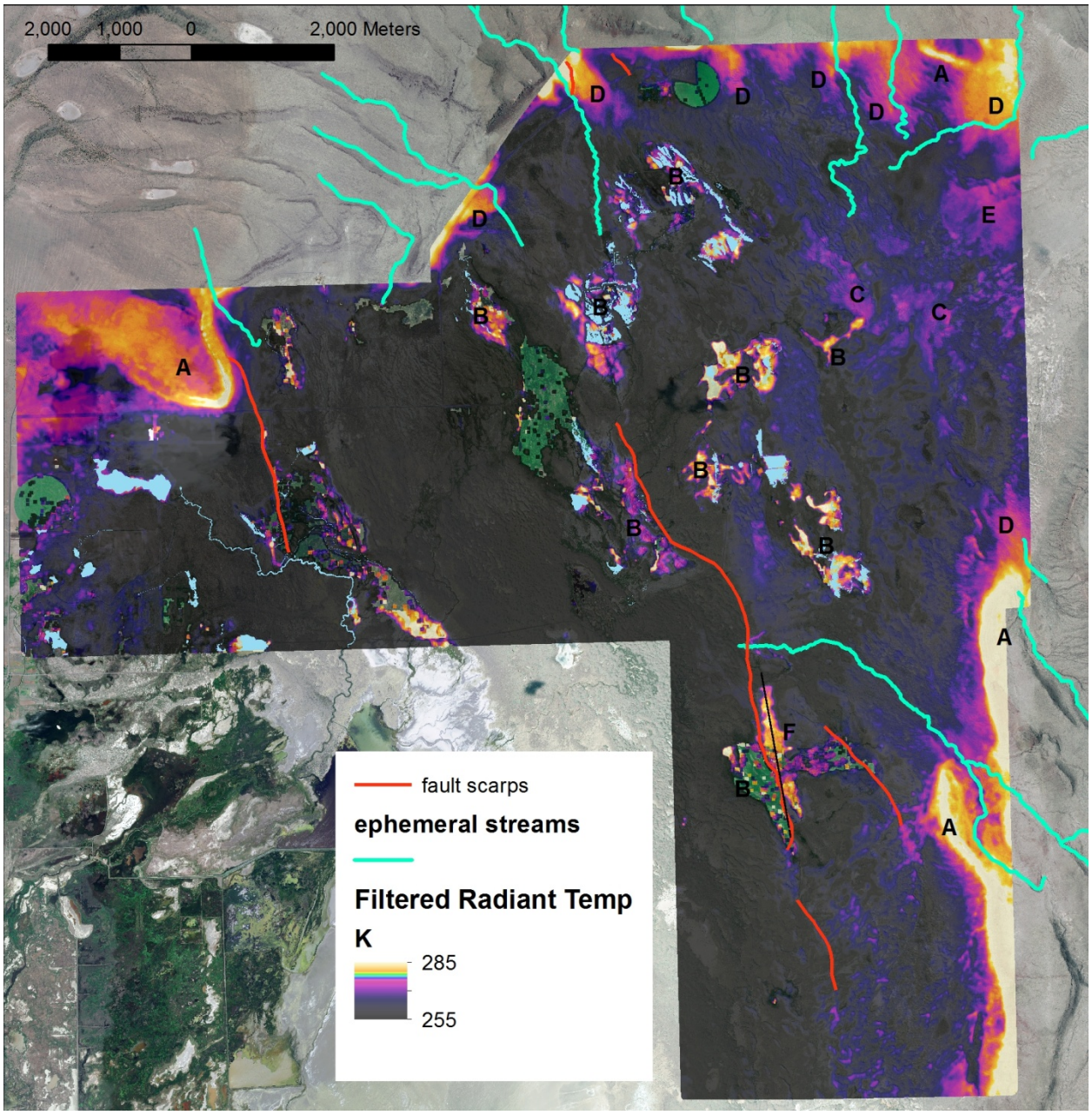

Figure 3.8: Masked and filtered TIR image. Letters mark temperature anomalies of different types. Water mask shown in light blue

more likely that these are due to incomplete masking of open water bodies. If masking were incomplete, there would remain relatively warm water pixels around the edge of the mask area that the filtering would restore to create areas of higher temperature. To illustrate this, we added the water mask to Figure 3.7 so that the relationship was more apparent. To prepare the water masks we used orthophotos collected in late spring through early fall, when surface water levels might have been lower than the mid-winter TIR acquisition window. To test this we compared the apparent water body extents implied by the lidar intensity imagery to the water mask derived from photos (Figure 3.9). The lidar instrument records the strength of signal return with

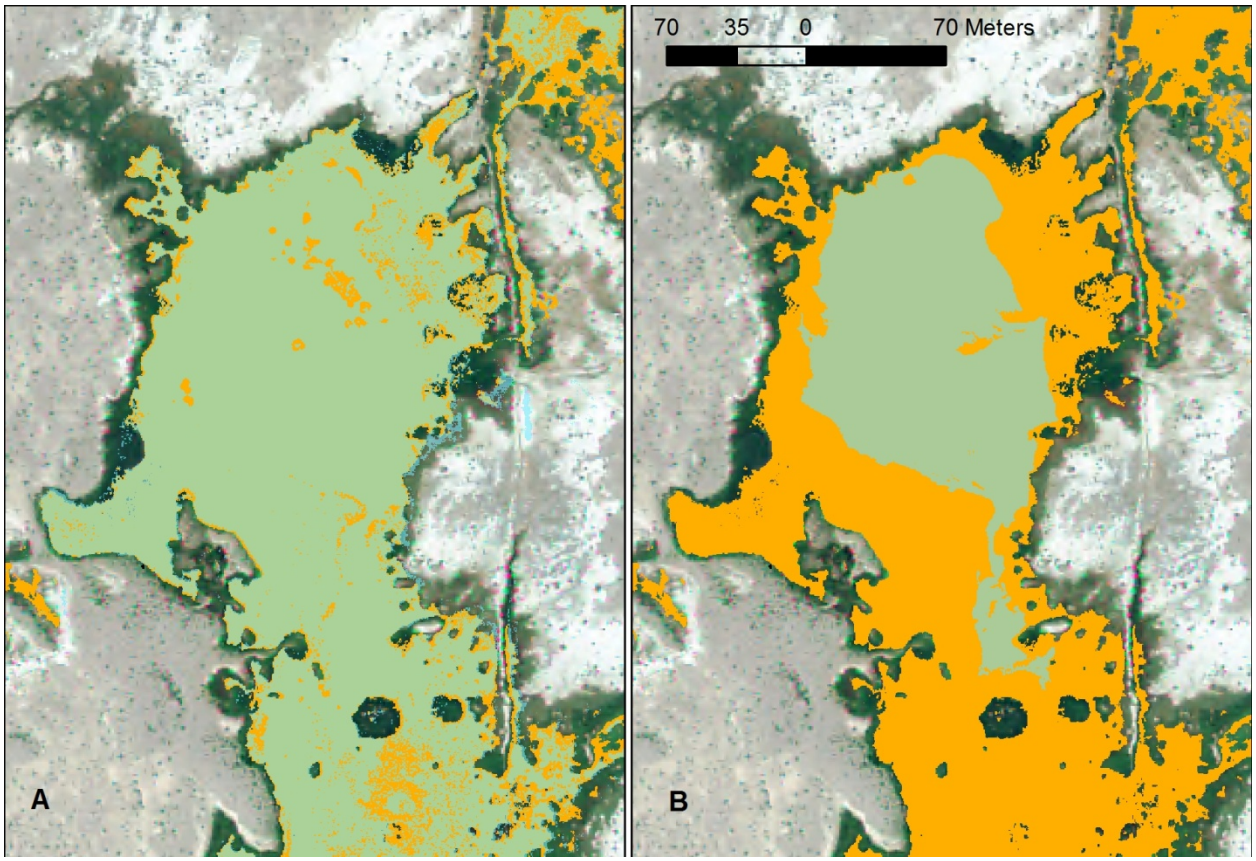

Figure 3.9: Comparison of water mask (light green tint, right image), and water area derived from low lidar intensity values (light green tint, left image. Orange color shows areas with T_r higher than 273 K, which are probably water. Orthophoto in background

each measurement pulse, building a map of reflectivity of the surface at lidar laser's wavelength of 1064 nm. At that wavelength water has a reflectivity of .07% (http://www.icess.ucsb.edu/modis/EMIS/html/em.html), far lower than virtually any other materials in the image. Hence it is possible to approximate the extent of water present during collection We checked this in a few areas, and found that the water coverage suggested by the lidar was consistently greater than our mask, which may explain the type B anomalies. The fact that the anomalies are typically close to freezing also suggests that they could be due to ice accumulated around water bodies. Ice also has a very low reflectivity at 1064 nm (0.5%) (http://www.icess.ucsb.edu/modis/EMIS/html/em.html)

Type C anomalies are restricted to the NE corner of the study area, and are typically 3-5 K above background. Type C anomalies are closely spatially associated with the edges of individual dunes groups of dunes or interdune pans, which suggests that they may be the result of emissivity difference rather than real ground temperature differences.

Type D anomalies occur along the N and E edges of the study area, generally along the playa floor adjacent to the bounding uplands. These anomalies are typically 5-8 K above background (up to 273 K), and are all located where an ephemeral stream from the highlands enters the valley floor. Figure 3.10 shows a close-up view of one of these anomalies, and the

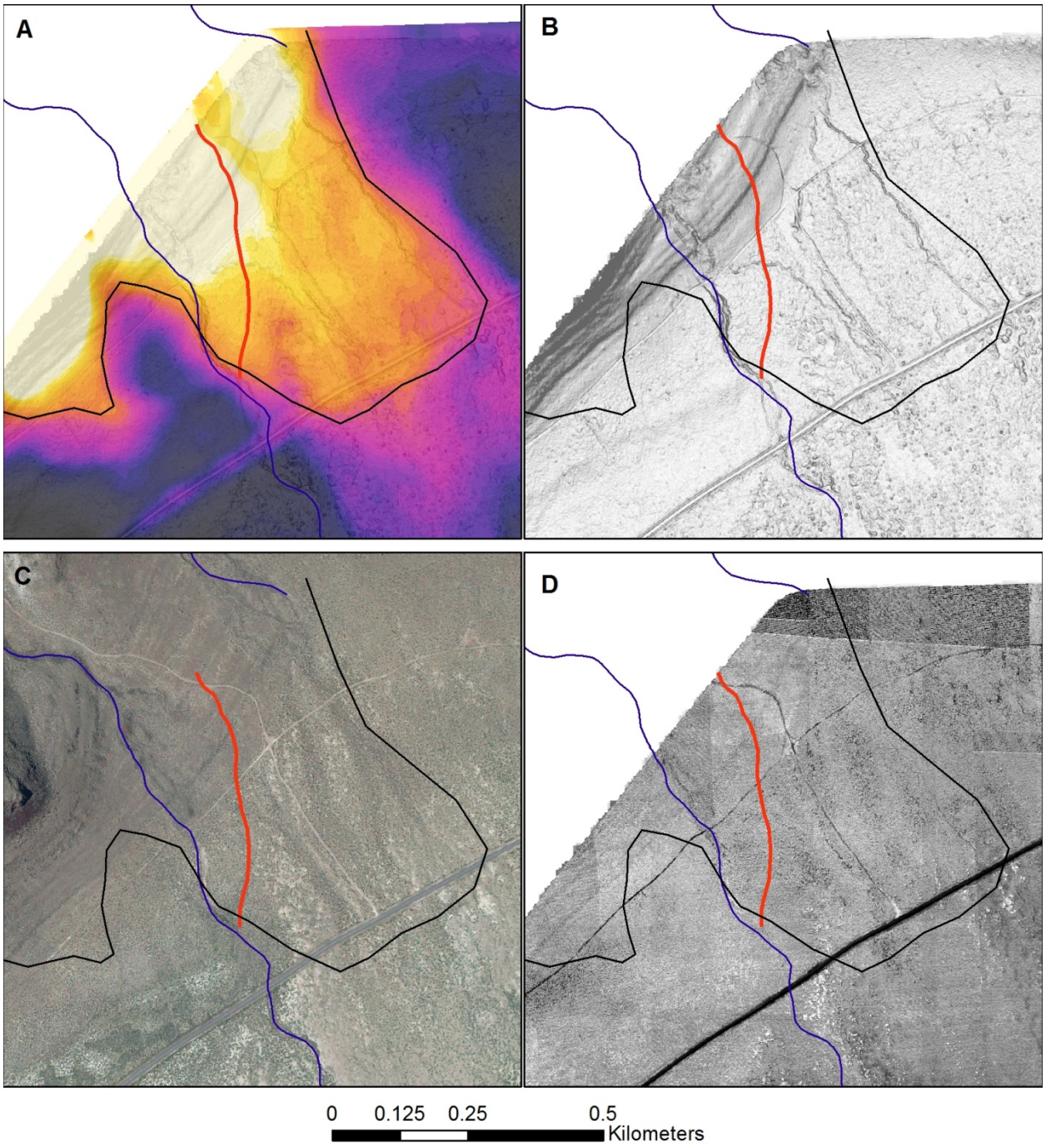

Figure 3.10: Detail of type D thermal anomaly. A, masked and filtered TIR, blue line is ephemeral stream course, red line fault scarp, black line approximate outline of thermal anomaly; B, lidar slopeshade; C, orthophoto; D, lidar intensity image

corresponding orthophoto and lidar image. Neither image shows any features that correspond to the edge of the thermal anomaly, suggesting that the anomaly is not the result of differences of emissivity in surface soils. We visited several of these anomalies in the field and photographed soils across the thermal anomaly boundaries and observed no systematic differences. We speculate that these anomalies may be due to the presence of relatively warm groundwater that is

being channeled down the ephemeral drainages and approaching the surface close enough to influence the ground temperature.

The single type E anomaly occurs in the NE corner of the study area and is about 3-5 K above background. It has the same relationship to dune topography that the Type C anomalies have, but also occurs at the mouth of an ephemeral drainage.

There is one type F anomaly that occurs in the S of the study area along the Summer Lake Fault (Figure 3.5, Figure 3.11). This anomaly is about 6-8 K above background, and is located on the up thrown side of the fault and is elongate parallel to the fault. Details of this anomaly are shown in Figure 3.11. There is very little water apparent in the anomaly area, either in the water mask developed from in the orthophoto (Figure 3.11-c) or in the water mask from lidar intensity imagery (Figure 3.11-b). It is also clear by comparing the orthophoto (Figure 3.11-c) and the masked T_r image (Figure 3.11-a), that there is abundant ground in the anomaly area that is relatively warm. As a result, we believe that this is a true ground temperature anomaly, not an artifact of poor masking of surface water. One cautionary note is that the northern half of the site has abundant mineral salts on the ground surface. This could be causing an apparent anomaly due to higher emissivity, but since the image is normalized to the relatively high emissivity of water, this is unlikely. The salts may be evidence of upwelling of groundwater, so the ground temperature anomaly may again be due to the presence of relatively warm ground water very near the ground surface.

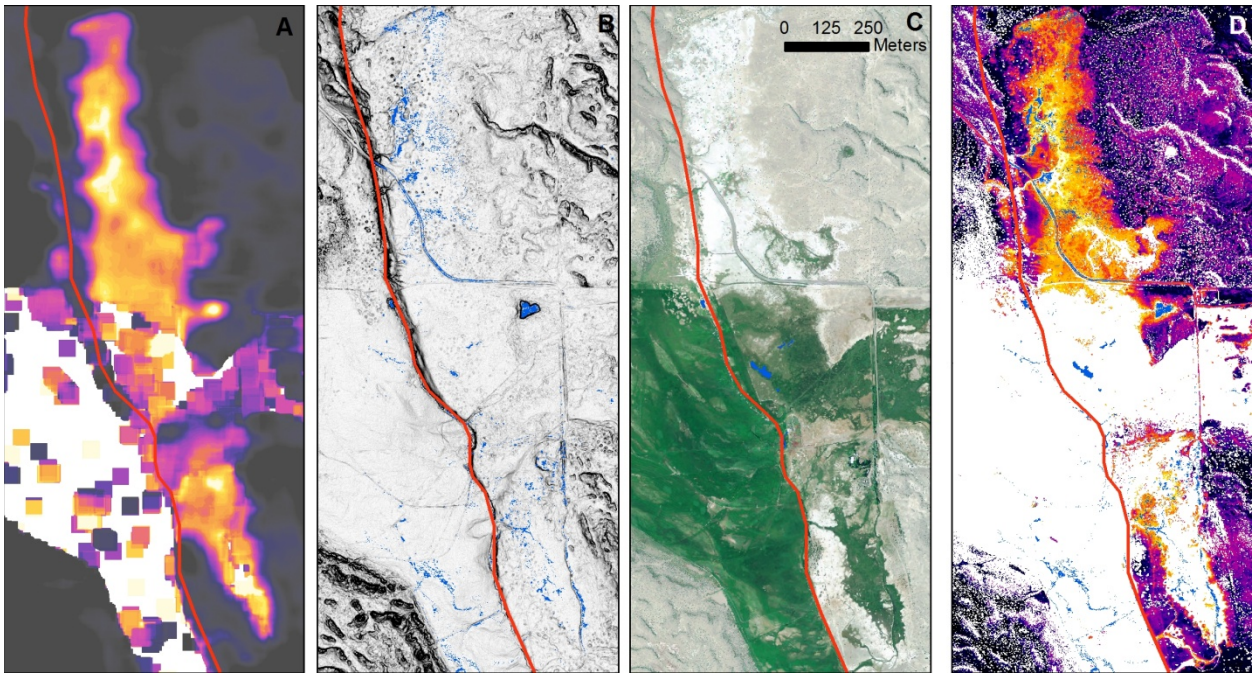

Figure 3.11: Detail of thermal anomaly F. A, masked and filtered Tr image; B lidar slopeshade with lidar intensity derived water/ice in blue; C, orthophoto with water mask in blue; D, masked TIR data

4.0 DISCUSSION

This experiment in the collection of high resolution, high accuracy TIR and lidar imagery for geothermal exploration has been generally successful. It is clear that it is possible to collect large swaths of very high quality data, and to achieve high spatial accuracy with the thermal imagery by using the lidar data to rectify it. The topographic and thermal imagery together have a resolution of about 1 m, and accuracy respectively of .01 m and .5 C.

It is also clear that the combined imagery is extremely effective at locating cold and warm springs, both on land and in water bodies. The data also allow accurate estimation of spring temperature, within the limited testing we were able to accomplish.

The lidar imagery is extremely effective at locating even very subtle Holocene fault scarps, and would be an indispensable tool for creating an accurate and detailed geologic map. Both of these characteristics are important to geothermal exploration.

The combined imagery was able to locate several low-thermal-amplitude, long-spatial-wavelength anomalies, several of which (types A, D and F) were almost certainly associated with true ground temperature differences (though not necessarily geothermal).

This pilot study has identified what we believe to be at least one significant exploration target. The area around thermal anomaly F (Figure 3.11) has one of the most convincing ground temperature anomalies, is associated with a Holocene fault with significant activity, and is associated with numerous warm springs. These observations are consistent with the presence of a geothermal circulation system associated with the fault that is bringing warm groundwater to the surface in the area of anomaly F.

Time and funding did not allow us to test these observations with more comprehensive measurement of spring temperatures or temperature gradient measurements in existing or purpose-drilled wells, or hand auger holes. We were also unable to carry out analysis of the other four areas of imagery that were collected in association with this larger project. It is notable that a temperature gradient hole (SL-1) drilled in the NW corner of the study area as part of a related project showed good evidence of a geothermal system at depth (Niewendorp, 2013). As can be seen in Figure 3.12, there is a warmer water zone (over 23°C) in SL-1 at approximately 220 ft below ground surface. The unusual profile of SL-1 maybe due to a strong counter flow of water at different temperatures in at least 3 different zones (lost circulation zones) in the well (David Blackwell, written communication, 7-1-2013).

We feel that these results warrant further study as described above, and if validated, may provide a mechanism for rapid screening of large areas for geothermal potential.

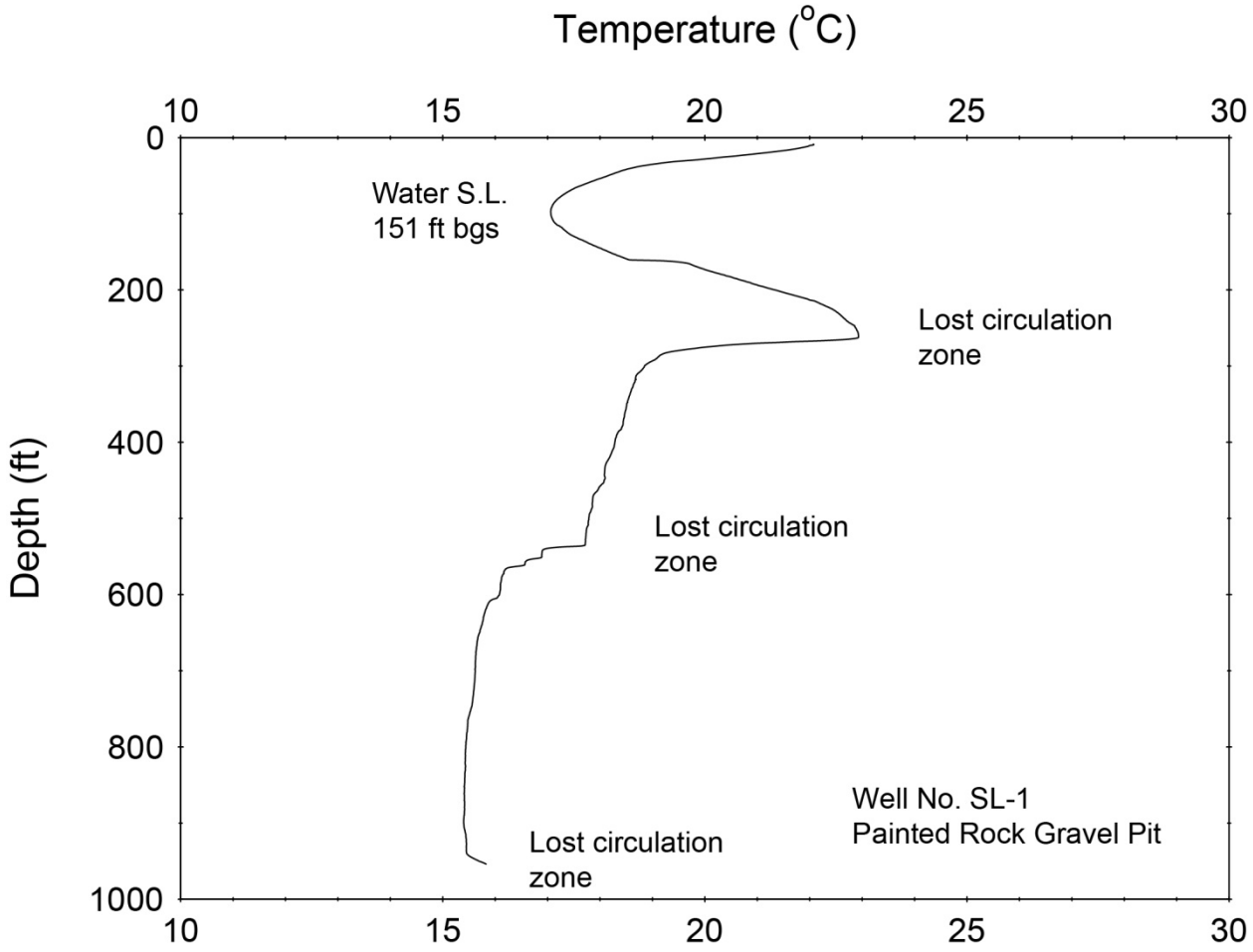

Figure 3.12: August 20, 2013 temperature profile of SL-1. There is a warmer water zone (over 23 C) at approximately 220 ft bgs

5.0 ACKNOWLEDGMENT

This material is based upon work supported by the Federal Department of Energy's (USDoE) Geothermal Technologies Office and between the Arizona Geological Survey (AZGS; Sponsor working on the behalf of the American Association of State Geologists (AASG)) and the Oregon Department of Geology and Mineral Industries (DOGAMI; Subrecipient) under Award Number(s): Prime Award No. DE_EE0002850 and Sub Award No. OR-EE0002850, American Recovery and Reinvestment Act of 2009. The contents of the report are disseminated in the interest of information exchange.

6.0 REFERENCES

Bennet, L., and Madin, I.P., 2012, Identification of a new fault and associated lineament features in Oregon's Summer Lake Valley using high-resolution lidar data: Abstract 1502-719 presented at 2012 Fall Meeting, AGU, San Francisco, Calif., 3-7 Dec.

Coolbaugh, M. F., Kratt, C., Fallacaro, A., Calvin, W.M., and Taranik J.V., 2007, Detection of geothermal anomalies using Advanced Spaceborne Thermal Emission and Reflection Radiometer (ASTER) thermal infrared images at Bradys Hot Springs, Nevada, USA: Remote Sensing of Environment 106(3), pp 350-359.

Eneva, M., Coolbaugh, M., and Combs, J., 2006, Application of satellite thermal infrared imagery to geothermal exploration in East Central California: GRC Transactions 30.

Haselwimmer, C., Prakash, A., and Hldmann, G., 2011, Geothermal Exploration at Pilgrim Hot Springs, Alaska Using Airborne Thermal Infrared Remote Sensing. Accessed from http://energy-alaska.wdfiles.com/local--files/pilgrim-hot-springs-project-phase-1/6_GRC_2011_article.pdf

Hellman, M.J. and. Ramsey, M.S., 2004, Analysis of hot springs and associated deposits in Yellowstone National Park using ASTER and AVIRIS remote sensing: Journal of Volcanology and Geothermal Research 135(1–2), pp 195-219.

Hodder, D.T., 1970, Application of remote sensing to geothermal prospecting: Geothermics 2, Part 1(0): 368-380.

Jacworowski, C., Heasler, H.P., Neale, C.M.U., and Sivarajan, S., 2009, Integrating lidar and airborne thermal infrared imager for geologic mapping of hot spring basin, Yellowstone National Park: Geological Society of America *Abstracts with Programs*, Vol. 41, No. 7, p. 433.

Kratt, C., Coolbaugh, M.F., and Calvin, W.M., 2006, Remote Detection of Quaternary Borate Deposits with ASTER Satellite Imagery as a Geothermal Exploration Tool: GRC Transactions 30.

Langridge, R.M., Pezzopane, S.K., and Weldon, R.J., 2001, Slip rate, recurrence intervals and paleoearthquakes for the Ana River Fault, Central Oregon; in Negrini, R., Pezzopane, S.K., and Badger, T., eds. Quaternary Studies near Summer Lake Oregon: Friends of the Pleistocene Ninth Annual Pacific Northwest Cell Field Trip, September 28-30, 2001. Accessed from http://sleipnir.cs.csubak.edu/~rnegrini/2001FOPSummerLakeGB.pdf

Lee, K., 1978, Analysis of thermal infrared imagery of the Black Rock Desert geothermal area: Q. Colo. Sch. Mines; (United States), 73(3), pp 31-43.

Licciardi, J.M., 2001, Chronoogy of latest Pleistocene lake-level flucturations in the pluvial Lake Chewaucan basin, Oregon, USA: Journal of Quaternary Science Vol. 16, pp 545-553.

Mongillo, M., 1994, Aerial Thermal Infrared Mapping of the Waimangu-Waiotapu Geothermal Region, New Zealand." Geothermics 23(5/6), pp 511-526.

Niewendorp, C.A. Ricker, T.R., Rabjohns, K.W., and Brodie, S.H., 2012, Geothermal Information Layer for Oregon, release 2 (GTILO-2): Oregon Department of Geology and Mineral industries Digital Data Series GTILO-2. Accessed from http://www.oregongeology.org/sub/gtilo/data/GTILO-Release-2.zip

Niewendorp, C.A., 2013, Thermal gradient drilling: Oregon Department of Geology and Mineral Industries ARRA Deliverable Report, p. 24. Accessed from http://www.oregongeology.org/sub/gtilo/data/supplemental/ARRA_Well_Drilling_Report.pdf

Niewendorp, C.A., English, J.T., Ferro, P.A., and Madin, I.P., 2013, Acquisition of airborne thermal infrared (TIR) and lidar imagery in central and eastern Oregon, Technical Specifications: Oregon Department of Geology and Mineral Industries ARRA Deliverable Report, p. 18. Accessed from http://www.oregongeology.org/sub/gtilo/data/supplemental/Using_Airborne_Thermal_Infrared.pdf

Olsen, R.C., 2007, Remote Sensing from Air and Space: Society of Photo-Optical Instrumentation Engineers Monograph 162.

Seielstad, C. and Queen, L., 2009, Thermal Remote Monitoring of the Norris Geyser Basin, Yellowstone National Park, Final Report for the National Park Service Cooperative Ecosystem Studies Unit, Agreement No. H1200040001, pp 38.

Vaughan, R. G., Calvin, W.M., and Taranik, J.V., 2003, SEBASS hyperspectral thermal infrared data: surface emissivity measurement and mineral mapping: Remote Sensing of Environment 85(1), pp. 48-63.